Journal of Colloid and Interface Science 653 (2024) 807–820

Contents lists available at ScienceDirect

Journal of Colloid And Interface Science

journal homepage: www.elsevier.com/locate/jcis

Interaction of impinging marangoni fields

Steven Iasella [a], Ramankur Sharma [a], Stephen Garoff [b], Robert D. Tilton [a,c,*]

[a] Department of Chemical Engineering, Center for Complex Fluids Engineering, Carnegie Mellon University, Pittsburgh, PA 15213, USA
[b] Department of Physics, Center for Complex Fluids Engineering, Carnegie Mellon University, Pittsburgh, PA 15213, USA
[c] Department of Biomedical Engineering, Carnegie Mellon University, Pittsburgh, PA 15213, USA

GRAPHICAL ABSTRACT

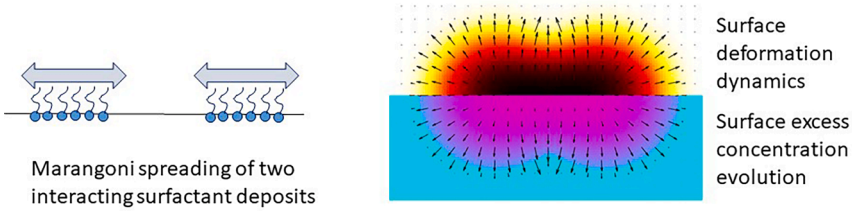

ARTICLE INFO

Keywords:
Solutal Marangoni flow
Surfactant
Surface tension
Transport phenomena
Numerical model

ABSTRACT

Hypothesis: Surface tension gradient driven Marangoni flows originating from multiple sources are important to many industrial and medical applications, but the theoretical literature focuses on single surfactant sources. Understanding how two spreading surfactant sources interact allows insights from single source experiments to be applied to multi-source applications. Two key features of multi-source spreading – source translation and source deformation – can be explained by transport modeling of a two-source system.

Modeling: Numerical simulations of two oleic acid disks placed at varying initial separation distances on a glycerol subphase were performed using COMSOL Multiphysics and compared to spreading of a single surfactant source.

Findings: Interaction of two spreading sources can be split into three regimes: the independent regime – where each source is unaffected by the other, the interaction regime – where the presence of a second source alters one or more features of the spreading dynamics, and the quasi-one disk regime – where the two sources merge together. The translation of the sources, manifested as increasing separation distance between disk centers of mass, is driven by the flow fields within the subphase and the resultant surface deformation, while deformation of the sources occurs only once the surfactant fronts of the two sources meet.

1. Introduction

Localized adsorption of surfactant on a liquid/vapor interface creates a surface tension gradient along the interface. The resulting Marangoni stresses cause the surface to deform and flow from low surface tension regions to high surface tension regions. This has been shown both experimentally for disks[1,2] and drops[3–5] of surfactants and theoretically for disks[6–9] and drops[10]. Such solutal Marangoni spreading phenomena are critical in a variety of applications including oil spill remediation[11], pulmonary drug delivery[3,5,12–17], and

* Corresponding author.
E-mail address: tilton@cmu.edu (R.D. Tilton).

https://doi.org/10.1016/j.jcis.2023.09.109
Received 10 July 2023; Received in revised form 9 September 2023; Accepted 17 September 2023
Available online 20 September 2023

various coating processes[18–20].

The case of a single source of surfactant spreading along a simple liquid subphase has been well-studied for a variety of conditions. Surface height profiles and surfactant distributions have been constructed for many different conditions resulting in a better understanding of the effects of subphase depth[8], spreading parameter[8], presence of pre-existing endogenous surfactant[12,21–24], surfactant solubility [3,10,25–27], subphase viscoelasticity[28], fingering instabilities [29,30], depletion of surfactant[31], surfactant synergism[14], and coupling of Marangoni and capillary waves[15]. While these fundamental studies provide detailed insights into Marangoni spreading, this prior research focused on single surfactant sources. It is yet unknown how the described behaviors would apply to the case of multiple surfactant sources as would occur, for example, in aerosol or spray delivery where a field of droplets is deposited. The mutual interaction of two impinging Marangoni spreading fields is not understood.

During a Marangoni spreading event the surface tension gradient is the driving force for spreading. At the surfactant front (the edge of the region of the surface where the surfactant is located), a shock-like distortion is formed[7]. The surface tension gradient is largest at the front, but the entire gradient is important for the flow behavior[1]. The resulting ridge moves out radially from the original region containing the surfactant[7,8]. There is liquid motion in front of the ridge and if the gravity parameter $G = \frac{\rho g H^2}{S}$ (where ρ is the suphase density, H is the subphase height, g is the gravitational acceleration, and $S = \gamma_o - \gamma_{source}$, with γ_o being the surface tension of the clean interface and γ_{source} being the surface tension in the surfactant source) is greater than 0.5, radial recirculation flows can form beneath the surface in the area of deposition[7,13].

There has been significantly less study of the spreading of droplet fields. A two-part experimental study conducted by Sharma, Khanal, and collaborators[16,17] examined the effects of aerosol deposition rate on the spreading of a field of surfactant-laden droplets. At high deposition fluxes the droplets coalesced after deposition and behaved as one large drop[17]. At lower deposition fluxes the droplets spread as a field of distinct droplets which behaved as a group[16] (see Supporting Information Figure S1). Specifically for this second case, nearby droplets became deformed (Figure S2) as they came into contact with each other, and it was unclear whether these drops deformed through their interactions after having deposited on the surface at approximately the same time or if instead one droplet deposited on top of another after the first to deposit had spread out. While that work marked the first step into understanding the spreading behavior of surfactant-laden aerosols, it cannot be easily related to the more well-defined single source experiments which give deeper understanding of why the systems behave as they do. There is a smaller body of literature focusing on the coalescence of viscous lenses on viscous subphases[32–35].

This study begins to bridge the knowledge gap between single and multiple source Marangoni spreading. We modeled the interactions of two disks of insoluble surfactant placed on an initially clean subphase. We tracked the changes in subphase velocity, surface deformation, and surface tension, varying distance between the disks and paying particular attention to the maximum and minimum interface heights during spreading. Also, we examined how the disks spread apart from each other and the deformation of each disk. The more complex flow fields which result from the coupled surfactant sources were also explored. This begins the process of connecting single source surfactant spreading behavior to the spreading of droplet fields relevant in pulmonary drug delivery and other aerosol or spray applications.

2. Methods: Problem formulation

We consider the spreading of two monolayer disks of surfactant on an initially flat liquid subphase with uniform height H_0 (Fig. 1) and origin at (x=0, y=0, z=0). The surfactant sources were located with their edges

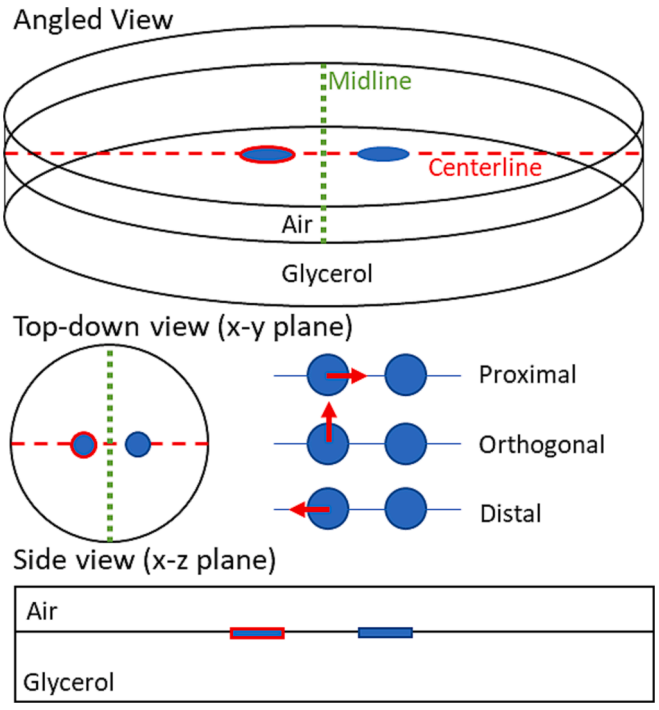

Fig. 1. Schematic of spreading simulation. Two fluid phases, a lower phase of glycerol and an upper phase of air. The blue circles show the location of the surfactant disks for the two disk case with the red outline on one of those disks indicating where the disk for the one disk case is located. The horizontal red dashed line is referred to as the centerline and the dotted vertical green line is referred to as the midline. The diagram also shows several directionalities used throughout the manuscript: Proximal (from the disk center along the centerline to the midpoint), distal (from the disk center along the centerline away from the midpoint), and orthogonal (from the disk center parallel to the midline. (For interpretation of the references to colour in this figure legend, the reader is referred to the web version of this article.)

separated by a distance d and had an initial surfactant distribution described by Equation 1[7] where Γ is the surfactant surface excess concentration, Γ_{max} is the maximum surface excess concentration, r_0 is the initial radius of the disk, and the Cartesian coordinate system is described by (x,y,z). For convenience when describing the disks, $r = \sqrt{(x \pm (d + r_0))^2 + y^2}$.

$$\Gamma(x, y, H_0) = \Gamma_{\max}\left(0.5\cos\left[\frac{\pi r}{r_0}\right] + 0.5\right)(r \le r_0) \quad (1)$$

$$0(r > r_0)$$

For illustrative purposes, the initial surfactant distribution (equation (1)) and the corresponding surface pressure distribution are plotted for one value of d in Supporting Information Figure S3. This construction allowed the disk of surfactant to have a smooth concentration profile (both continuous and continuously differentiable) connecting the initially surfactant-free surface regions to the surfactant-rich disk where the surfactant had an initial surface excess concentration Γ_{max} at the center of the disk. The size of the "dish" containing the liquid was set to $r_{wall} = d/2 + 25\ r_0$, far enough that the edge of the domain did not significantly affect the Marangoni spreading during the times studied, thus minimizing extrinsic effects of dish size. This also represents the dishes typically used to contain subphases in experimental work on the subject. To model the one disk case, only one of the disks (located at $x <$ 0) had surfactant in it at the initial time with the other having a surface excess concentration of zero. Fig. 1 also describes three key directions discussed throughout the manuscript: proximal (from one disk center

along the centerline toward the midpoint between the two disks), distal (from one disk center pointing away from the other disk along the centerline), and orthogonal (from one disk center perpendicular to the centerline). As in previous work on a single disk[7], the surface equation of state was constructed by fitting experimental data for oleic acid on a glycerol subphase reported by Sinz and co-workers[36] to Equation (2), giving an empirical expression for the relationship between the surface excess concentration and the surface tension,

$$\gamma = \gamma_{min} + \pi_{max} e^{-A\left(\frac{\Gamma}{\Gamma_{max}}\right)^2} \tag{2}$$

where γ is the surface tension, γ_{min} is the minimum surface tension achieved at Γ_{max}, π_{max} is the maximum surface pressure ($\pi_{max} = \gamma_o - \gamma_{min}$, the reduction of surface tension achieved by the surfactant at Γ_{max}), and A is a fitting parameter specific to the surfactant and subphase (A = 6.125 for oleic acid on glycerol). Glycerol was chosen as the subphase, as its viscosity is sufficiently large to dampen the capillary waves that would otherwise be launched by the Marangoni stress[14,15], thereby matching most of the prior theoretical literature. Although we adopt a particular equation of state (Equation (2) and subphase, the basic features of Marangoni spreading for a single source do not depend on the properties of the surfactant system.[3,15,37] Thus, the general features described here for two sources are expected to be relevant to two-source Marangoni spreading in a variety of systems. We have made the standard assumption of microscopic reversibility, whereby the instantaneous local surface tension is dictated by the local surface excess concentration according to the equilibrium equation of state at all times during the dynamic spreading event.

The Navier-Stokes equation (Equation (3), continuity equation (Equation (4), and surface transport equation (Equation (5) were used to describe the transport of the glycerol subphase and a thin layer of air above the liquid surface (set to a thickness of $H_0/2$, whereby the upper boundary of the air layer was located at ($H_{air} = 1.5\ H_0$).

$$\rho\left(\frac{\partial \overline{u}}{\partial t}\right) + \overline{u}\cdot\overline{\nabla}\overline{u} = -\overline{\nabla}P + \mu\nabla^2\overline{u} + \rho g \tag{3}$$

$$\overline{\nabla}\cdot\overline{u} = 0 \tag{4}$$

$$\frac{\partial \Gamma}{\partial t} + \overline{\nabla}_s\cdot\left(\Gamma\overline{u}|_{z=H}\right) = D_s\nabla_s{}^2\Gamma \tag{5}$$

In Equations (3) – (5), $\overline{u}$ is the fluid velocity, μ is the fluid viscosity, t is time, P is the pressure, $\overline{\nabla}$ is the three dimensional gradient operator, $\overline{\nabla}_s$ is the surface gradient operator, H is the height of the interface, and D_s is the surface diffusion coefficient. As the Mach number is always below 0.1 during a spreading event, we neglected the compressibility in both fluid phases.

Boundary conditions were defined for the bounding surfaces and the interface between the subphase and air layers. No-slip boundary conditions were imposed at the bottom of the dish and the top of the air phase:

$$\overline{u}|_{z=0,H_{air}} = 0 \tag{6}$$

Around the edge of the dish, a Navier slip condition was imposed at the three-phase contact line on the container wall in order to avoid a velocity discontinuity and the associated unbounded tangential force on the wall exerted by the interface[38],

$$\overline{\overline{T}}_{fluid}\cdot\hat{n}_{wall} = -\frac{\mu}{\beta}\overline{u} \tag{7}$$

where $\hat{n}_{wall}$ is the unit normal vector to the container wall, $\overline{\overline{T}}_{fluid}$ is the stress tensor for the liquid, $\overline{\overline{T}}_{fluid} = -P\overline{\overline{I}} + \mu\left(\overline{\nabla}\overline{u} + \overline{\nabla}\overline{u}^T\right)$, P is the isotropic pressure, $\overline{\overline{I}}$ is the identity matrix, and β is the slip length, set to 0.2 $h_{element}$, where $h_{element}$ is the mesh element size in the numerical solution of the model. This allowed the stress tangential to the wall at the three-phase contact line to be proportional to the tangential velocity of the liquid. The contact angle of the liquid at the wall is set to θ = 90°, though recent work shows that this contact angle does not significantly affect the Marangoni spreading behavior[14]. A no-flux condition was imposed at the outer wall of the container normal to the outer wall both for the fluids (Equation (8) and the surfactant (Equation (9):

$$\overline{u}|_{x^2+y^2=r_{wall}{}^2}\cdot\hat{n}_{wall} = 0 \tag{8}$$

$$\overline{\nabla}\Gamma|_{x^2+y^2=r_{wall}{}^2}\cdot\hat{n}_{wall} = 0 \tag{9}$$

At the fluid/air interface, continuity of velocity (Equation (10) and a stress balance (Equation. (11)), were imposed:

$$\overline{u}_{fluid}\big|_{z=h} = \overline{u}_{gas}\big|_{z=h} \tag{10}$$

$$\hat{n}\cdot\left(\overline{\overline{T}}_{air} - \overline{\overline{T}}_{fluid}\right) = \sigma\hat{n}\left(\overline{\nabla}_s\cdot\hat{n}\right) - \overline{\nabla}_s\sigma(z=h) \tag{11}$$

where $\hat{n}$ is the unit normal vector to the liquid surface.

The simulations were carried out with COMSOL Multiphysics 5.1 using a transient study and the two phase flow, moving mesh and general form PDE physics modules. This approach uses the arbitrary Lagrangian-Eulerian (ALE) finite element method to calculate the surface shape and species transport by locating the surface at mesh points in the simulation, which are allowed to change position with time. Times ranging from 0.0001 to 2000 s were simulated, and 75 data points were recorded within every decade of time with a relative error[39] of 10^{-5}. Values used for the parameters are reported in Table S1.

While most dimensionless parameters were held constant during the simulations, the values of these parameters are useful for understanding the broad behavior of the system (Table S2). The aspect ratio (subphase depth/radius of the surfactant disk) was 0.4. For very small aspect ratios, the lubrication approximation can be used to simplify the transport equations[7,8]; however, as the value was fairly large in this case in order to match conditions commonly used in experiments, the lubrication approximation would not be appropriate. This necessitated the use of a simulation method such as ALE. The Peclet number ($Pe = \frac{SH_0}{\mu D_s}$) was ≫ 1, so the convective Marangoni transport would be much more important than surfactant diffusion. The gravity parameter ($G = \frac{\rho {H_0}^2 g}{S}$)was of order 10, indicating that recirculation flows would be expected to occur [7,8,13] and prevent dewetting of the substrate. The Reynolds number ($Re = \frac{SH_0\rho}{\mu^2}$) was ≪ 1, so viscous forces would dominate the inertial forces. The Marangoni number ($Ma = \frac{{H_0}^2}{R_0}\frac{\gamma_{min}}{S}$) was 0.19 , so the Marangoni and capillary stresses would both contribute to stresses at the surface, with the Marangoni stresses generally exceeding capillary stresses.

3. Results and discussion

We first present and describe snapshots of important events that occur during spreading. Once the general behaviors of the two spreading disks have been established, we will more carefully examine how key properties change with direction and time. Finally, we will discuss the difference between lateral disk translation (disks moving away from each other) and deformation (changes in shape) as well as the effects of the initial separation distance on the spreading behavior. Nomenclature for directionality was indicated in Fig. 1, with additional terms describing position defined in Figure S4.

3.1. Spreading behavior for the two-disk system

The simulation of two spreading surfactant disks was performed for initial edge separation distances of d/r_o = 1, 2, 3, 4, and 5. An animation

of the overall spreading behavior for $d/r_o = 2$ is provided in Figure S5. To analyze the complex behavior of the system, key properties of the spreading event will be examined at different time points representative of different spreading regimes with distinct characteristics. Figs. 2 - 6 show the evolution of subphase height, surface excess concentration, and velocity fields during the spreading process. These results naturally divide the behavior of the system into three distinct regimes: the independent regime (Fig. 2), the interaction regime (Figs. 3 – 5), and the quasi-one disk regime (Fig. 6). Each figure includes direct comparisons of the surface height profile and surfactant surface excess concentration profile for the two-disk situation with those for the one-disk situation modeled separately at the same time point. Each of these figures were generated with a separation of $d/R_0 = 2$. However, the key trends were similar for all separation distances tested, with larger separation distances leading to characteristic regime transitions happening at later times, and with decreased magnitudes of the effects caused by the two-disk interaction: consequences of two-disk interactions were progressively delayed and attenuated with increasing initial disk separation distance. The effects of initial separation distance will be summarized at the end of the Results and Discussion section. The results will also show how the velocity fields and subphase deformation are related and propagate faster than the surfactant surface concentration (and corresponding surface pressure) gradients that drive them.

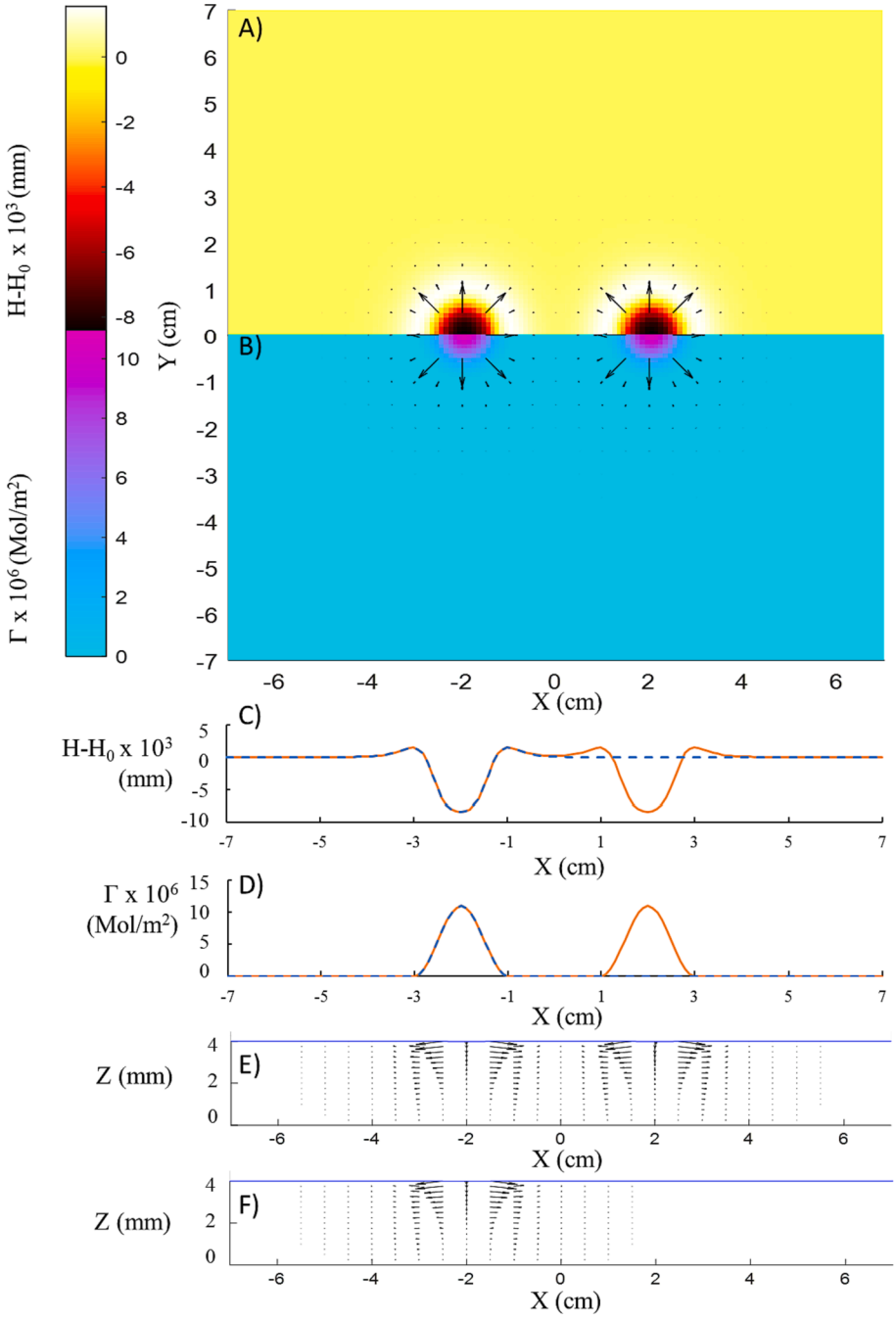

Fig. 2. Independent Regime, illustrated at t = 0.006 s. From top to bottom: top-down view heatmap of surface deformation (A), top down view heatmap of surface excess concentration (B), surface deformation along the centerline (C), surface excess concentration along the centerline (D), velocity field along the centerline for two disk case (E), and velocity field along the centerline for one disk case (F). The initial disk edge separation was $d = 2.0$ cm in the two-disk case. For C and D the solid line shows the two disk case while the dashed line show the one disk case. Largest velocity arrows in panels E and F are 4.2×10^{-3} m/s.

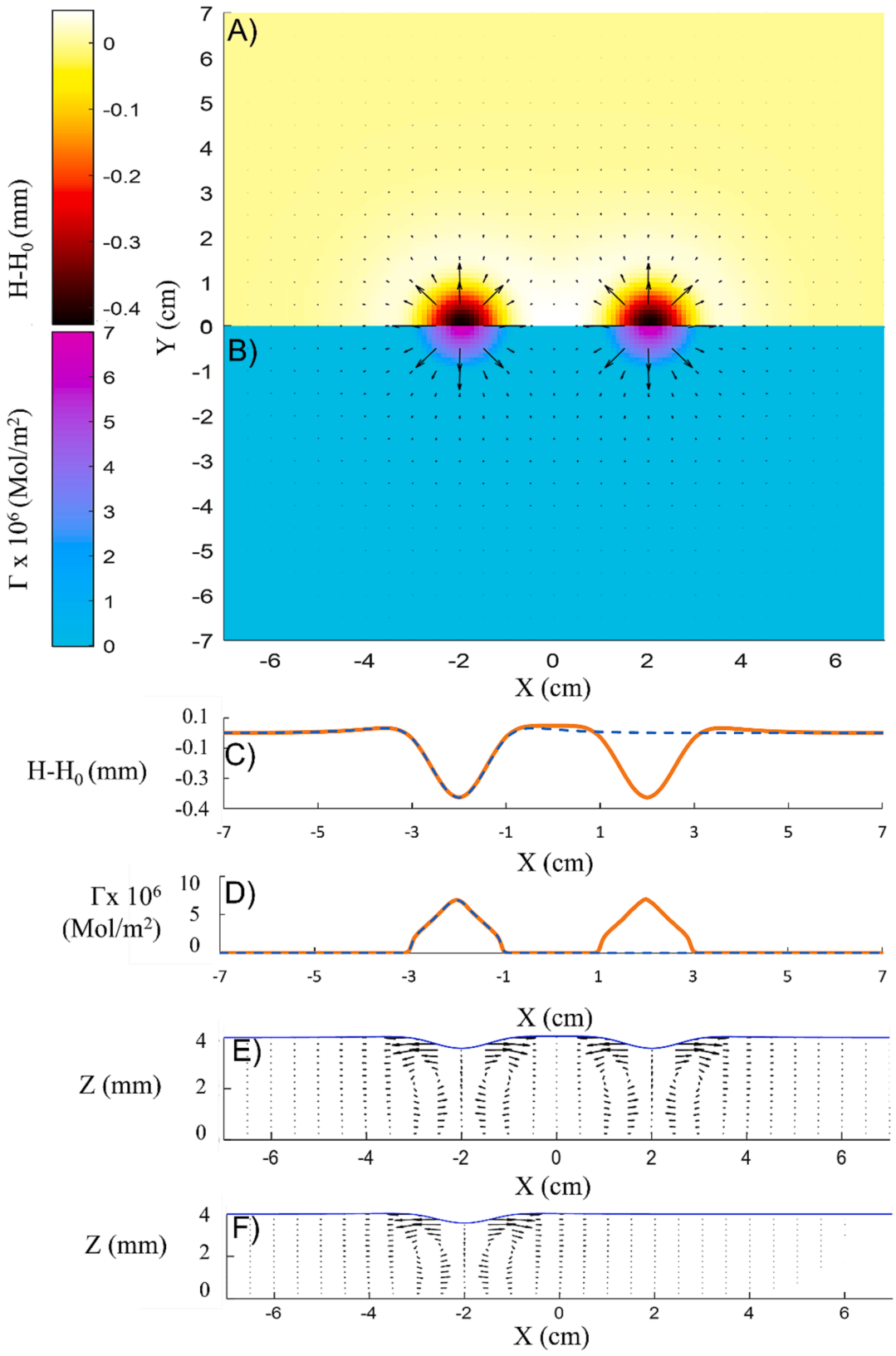

Fig. 3. The Interaction regime illustrated at 0.6 s. From top to bottom: top down view heatmap of surface deformation (A), top down view heatmap of surface excess concentration (B), surface deformation along the centerline (C), surface excess concentration along the centerline (D), velocity field along the centerline for two disk case (E), velocity field along the centerline for one disk case (F). The initial disk edge separation was d = 2.0 cm in the two-disk case. For C and D the solid line shows the two disk case while the dashed line shows the one disk case. Largest velocity arrows in panels E and F are 1.5x10^{-3} m/s.

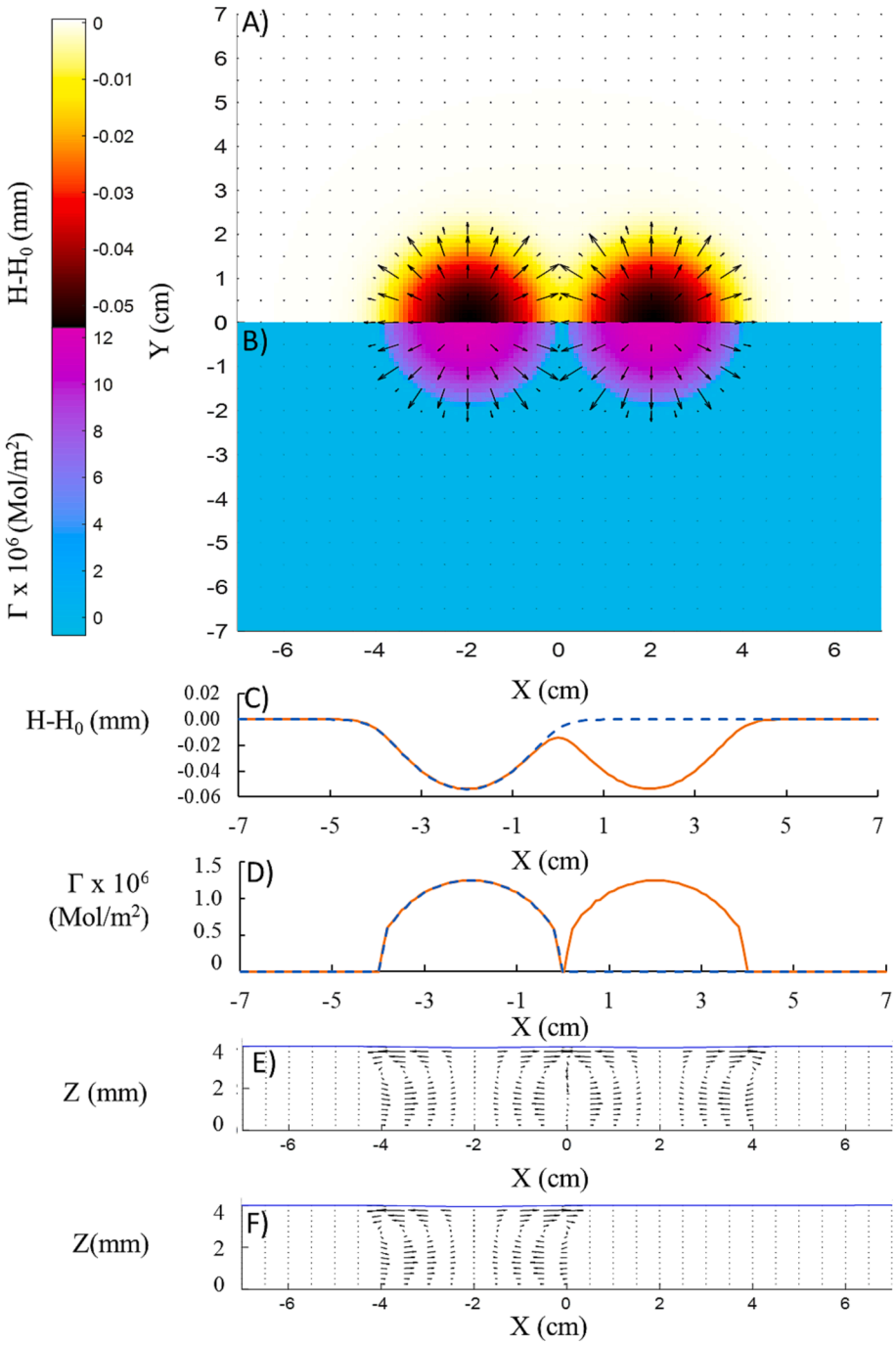

Fig. 4. The Interaction regime illustrated at 30 s. From top to bottom: top down view heatmap of surface deformation (A), top down view heatmap of surface excess concentration (B), surface deformation along the centerline (C), surface excess concentration along the centerline (D), velocity field along the centerline for two disk case (E), velocity field along the centerline for one disk case (F). The initial disk edge separation was d = 2.0 cm in the two-disk case. For C and D the solid line shows the two disk case while the dashed line shows the one disk case. Largest velocity arrows in panels E and F are $8.5x10^{-5}$ m/s.

3.1.1. The independent regime

The independent regime occurred at the earliest times, before the two disks significantly interacted with each other. Initially, a disk of radius 1 cm was placed at x = -2 cm (for the one-disk case) or two disks at $x = \pm 2$ cm (for the two-disk case). Heatmaps of the surface height and surface excess concentration show distinct circles for the two disks (Fig. 2A and B). The surface deformation defined as $H\text{-}H_0$ (Fig. 2C) and surface excess concentration profiles (Fig. 2D) measured along the midline of the disks, were indistinguishable for the one- and two-disk cases (see $x < 0$ region), and all disk features were symmetrical about their centers. (See Figure S6 for corresponding surface pressure distributions.) The scope of the comparisons are restricted to $x < 0$ because for $x > 0$ the mere presence of the second disk means that there are trivial differences not related to the interaction of the Marangoni sources. Marangoni spreading caused a depression in the surface height, i.e., a negative surface deformation, in the central part of the disk, surrounded by an outwardly moving ridge, as has been well established in the prior literature[7,8,13]. The Marangoni ridge (observed in Fig. 2C as the surface deformation maxima at $x \simeq \pm 3$ cm and $x \simeq \pm 1$ cm) was slightly further from the center of each disk than the surfactant front (defined as the position where the surface excess concentration fell below 0.01 % of Γ_{max} in Fig. 2D). The Marangoni ridge

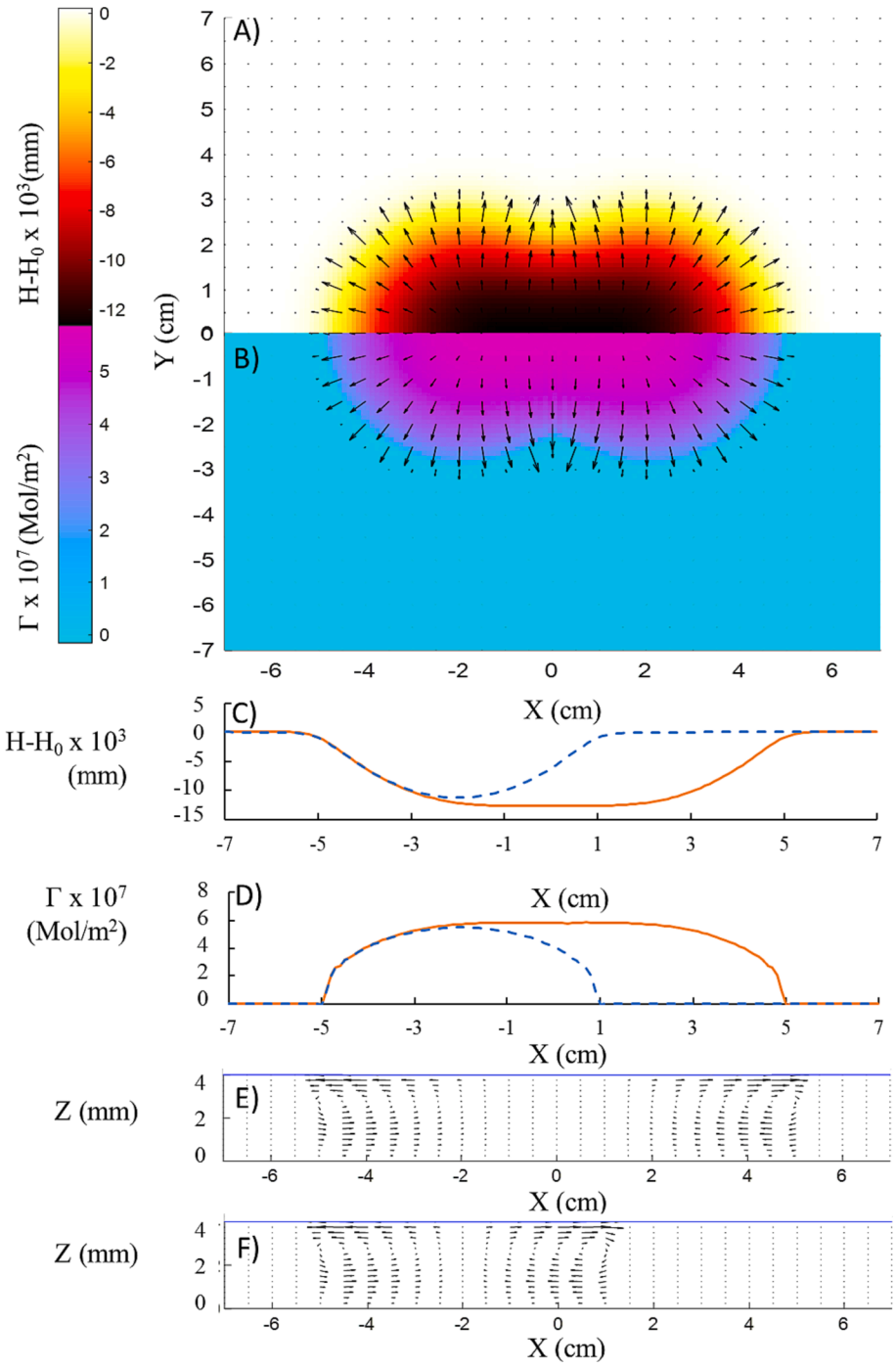

Fig. 5. The Interaction regime illustrated at 100 s. From top to bottom: top down view heatmap of surface deformation (A), top down view heatmap of surface excess concentration (B), surface deformation along the centerline (C), surface excess concentration along the centerline (D), velocity field along the centerline for two disk case (E), velocity field along the centerline for one disk case (F). The initial disk edge separation was d = 2.0 cm in the two-disk case. For C and D the solid line shows the two disk case while the dashed line shows the one disk case. Largest velocity arrows in panels E and F are 1.3×10^{-5} m/s and 1.4×10^{-5} m/s, respectively.

advanced ahead of the surfactant front throughout the entire extent of the simulation. The midline velocity field (Fig. 2E) showed symmetrical outward flow around the initial disk centers (positioned at $x = \pm 2$ cm) and was similar to the flow behavior for the one disk case (Fig. 2F). The flow behavior was consistent with the shape of the surface, as the growing depression in the center with a surrounding ridge coincided with a net outward flow from the initial disk location. The two-disk situation is simply a linear combination of individual one-disk spreading behaviors in the independent regime. This will not be true in the subsequent regimes.

3.1.2. The interaction regime - maximum height at midpoint: Marangoni ridge interaction

Whereas the independent regime yielded little symmetry breaking around the disk center for $x < 0$, the interaction regime was characterized by significant breaking of symmetry in the surface deformation on the distal and proximal sides of a disk. Key behaviors are depicted here at three distinct times within the interaction regime that are important to the overall spreading event: when a global maximum in suphase deformation occurred at the midpoint between the two disks (Fig. 3, $t \sim 0.6$ s), when the surfactant fronts from each disk met at the

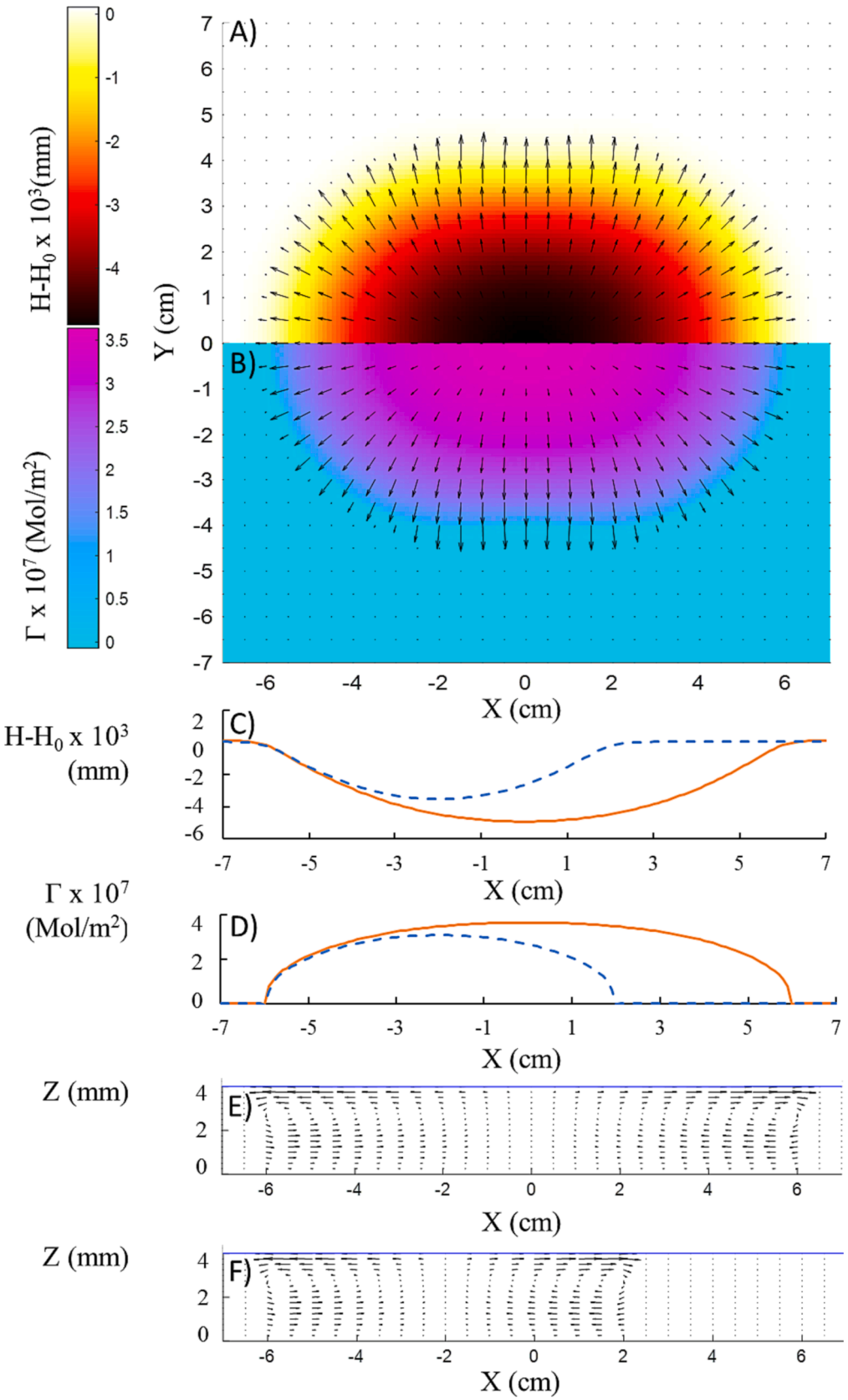

Fig. 6. The Quasi-one disk regime illustrated at 2000 s. From top to bottom: top down view heatmap of surface deformation (A), top down view heatmap of surface excess concentration (B), surface deformation along the centerline (C), surface excess concentration along the centerline (D), velocity field along the centerline for two disk case (E), velocity field along the centerline for one disk case (F). The initial disk edge separation was d = 2.0 cm in the two-disk case. For C and D the solid line shows the two disk case while the dashed line shows the one disk case.. Largest velocity arrows in panels E and F are 3.5×10^{-6} m/s and 3.3×10^{-6} m/s, respectively.

midpoint (Fig. 4, $t \sim 30$ s), and when a global *minimum* height occurred at the midpoint between the disks (Fig. 5, $t \sim 100$ s).

The maximum height at the midpoint occurred shortly after the two Marangoni ridges collided (0.6 s) at the midpoint between the two disks, as can be seen by the maximum deformation in Fig. 3A and C occurring at the midpoint and deviating slightly from the one disk case. It is important to note while the height profile reached a global maximum here, the surfactant fronts from the two disks had yet to interact (Fig. 3B and D) and were nearly identical to the one disk case (compare curves for $x < 0$). (See Figure S6 for corresponding surface pressure distributions.) The flow profile (Fig. 3E) along the centerline exhibited the beginning of the recirculation flows typical in Marangoni flows on deep subphases (seen in Fig. 3E and 4F where along a vertical set of arrows, those near the top of the subphase point away from the disk center and those near the bottom point toward it). The flows were still largely symmetric about the initial disk centers ($x = \pm$ 2 cm). The flow fields near each disk were still qualitatively similar to the field for the one disk case (Fig. 4F).

3.1.3. The interaction regime - surfactant front interaction at midpoint

As time proceeded, the next major feature to arise during the interaction regime was when the two surfactant fronts made contact at the midpoint (Fig. 4, $t = 30$ s). The edges of the surfactant front just touched each other (extending to precisely the midpoint, $x = 0$ cm, in Fig. 4B and D), however, the surface excess concentration profiles were still similar for the one disk and two disk cases: compare curves for $x < 0$. (See Figure S6 for corresponding surface pressure distributions.) We define that surfactant front interaction has occurred when the surface excess concentration at the midpoint increases beyond 0.01 % of Γ_{max}. The surface deformation at the midpoint, which had produced a global maximum at the previously shown time point (Fig. 3, $t = 0.6$ s), had now begun to decrease and become negative at $t = 30$ s (Fig. 4A and C). The most negative surface deformations were still located near the initial centers of the surfactant disks (at $x = \pm 2$ cm). Notably, the surface deformation at the midpoint had gone from being positive for the one disk case, to negative for two interacting disks. As time further progressed, the difference in the deformation between the one and two disk cases at the midpoint continued to increase. Though subtle, the proximal and distal recirculation fields (Fig. 4E) were no longer symmetric around the disk center. The velocity arrows at $x = 0$ cm were smaller in magnitude than those at $x = 4$ cm because the flow near the midpoint was impeded by the flow field generated by the second disk. The distal recirculation flow for the two-disk case ($x <$ -2 cm) was very similar to the one disk case (Fig. 4F) while the proximal recirculation (-2 cm $< x <$ 0 cm) flow showed the same subtle compression near the midpoint ($x =$ 0 cm). As we continue forward in time these differences between the distal originating flow field and the proximal originating flow field will continue to increase.

3.1.4. The interaction regime - minimum height at midpoint: merging of concentration profiles

With further progression of time, the last key feature of the interaction regime to develop was the appearance of a global minimum in surface deformation at the midpoint (Fig. 5, $t = 100$ s). From the surface deformation profiles, (Fig. 5A and C) the most negative deformation was now at the midpoint between the two disks rather than the disk centers, and the proximal and distal deformation profiles now both deviated from the single disk case for $x >$ -3 cm (Fig. 5A and C). The surface concentration profiles had now begun to merge, (Fig. 5B and D) and there was now a maximum in surface excess concentration (with a value $\sim$ 5 % of Γ_{max}) at the midpoint between the two disks (Fig. 5B). (See Figure S6 for corresponding surface pressure distributions.) Comparing Fig. 4E with 5E shows that the distal originating recirculation flow had extended towards $x = 0$ cm (recirculation can be seen in the arrows at $x =$ -2cm), and the proximal recirculation flow had been significantly disrupted (flow was significantly lessened in this region). Comparing the velocity fields for the one disk (Fig. 5F) case shows how much the proximal recirculation flows have been weakened by the interaction of the two opposing flow fields.

3.1.5. Quasi-one disk regime

After the interaction regime, all key features of the two disks started to merge and behave as if they were one combined, nearly elliptical, source, as shown in Fig. 6 for $t = 2000$ s. The surface distortion profiles (Fig. 6A and C), surfactant fronts (Fig. 6B and D), and two-disk velocity field (Fig. 6E) were all centered at the midpoint. (See Figure S6 for corresponding surface pressure distributions.) Deformation profiles were monotonically decreasing centered around the midpoint (Fig. 6A) as opposed to two deformed but distinct disks that existed at earlier times. The surfactant disks had merged into one nearly elliptical source. The proximal originating recirculation flow had ceased and the distal originating recirculation flow had extended all the way to the midpoint (flow was outward near the top of the subphase and directed inward toward the midpoint near the bottom of the subphase). In this quasi-one disk regime, the overall flow field resembled that of the one-disk flow field, but with an increased span along the centerline. The span of these recirculation flows was more extensive than that generated for the one disk case. At this point, all profiles and fields had deviated from the one disk case, but still resembled the flow in the distal direction for $x <$ -5 cm. The velocity fields between the one and two disk cases were nearly identical for $x <$ -4 cm.

To summarize, three key features characterize Marangoni spreading: the surface deformation, the surface excess concentration (and corresponding surface pressure) distribution, and the velocity field in the subphase. The velocity fields and subphase deformation are closely related to each other, and two disk interactions manifested at earlier times for these properties than for the surface excess concentration distribution that drives them. At early times, before any of the features interact, each disk behaves as a single, independent surfactant source of the same size. The first features to interact are the surface height distortion profiles and the velocity fields, indicated by a maximum distortion at the center and the deviation of the recirculation flows on either side of the disk. At these times, recirculation flows are still centered about the center of each disk. Eventually, the height distortion at the midpoint begins to decrease and the surfactant fronts meet at the midpoint, followed by the midpoint distortion achieving a minimum. At very late times, the surface excess concentration (and corresponding surface pressure) reaches a maximum at the midpoint and the recirculation flows become centered at the midpoint between the disks. The overall evolution of the disk shapes is consistent with the experimental observations in Figures S1 and S2. Next, we examine the temporal and directional dependence of key features in more detail.

3.2. Temporal evolution of spreading characteristics

3.2.1. Formation of recirculation flows at the midpoint

Flow fields in Figs. 3-6 were shown in the direction along the centerline connecting the two disks (distal and proximal directions). Fig. 7 shows the development of a recirculation flow in the orthogonal direction. For the midpoint between the two disks (at $x = 0$, shown in Fig. 7A-C), at early times in the interaction regime, the flow was all outward from the midpoint (Fig. 7A) but recirculation flows had already developed in the plane passing through the center of a disk in the orthogonal direction for the one- and two-disk cases (at $x =$ -2 cm, Fig. 7D for the two disks and Fig. 7G for the one disk case). Later in the Interaction regime ($t = 30$ s), an orthogonal recirculation flow had begun to develop at the midpoint (Fig. 7B) but was significantly weaker than the flow in the orthogonal direction in the plane passing through the center of a disk for the one- and two-disk cases (Fig. 7E and H). Finally, even later into the interaction regime ($t = 300$ s) the full recirculation flow had developed (Fig. 7C). The orthogonal recirculation flow that developed was nearly identical to the flow in the plane passing

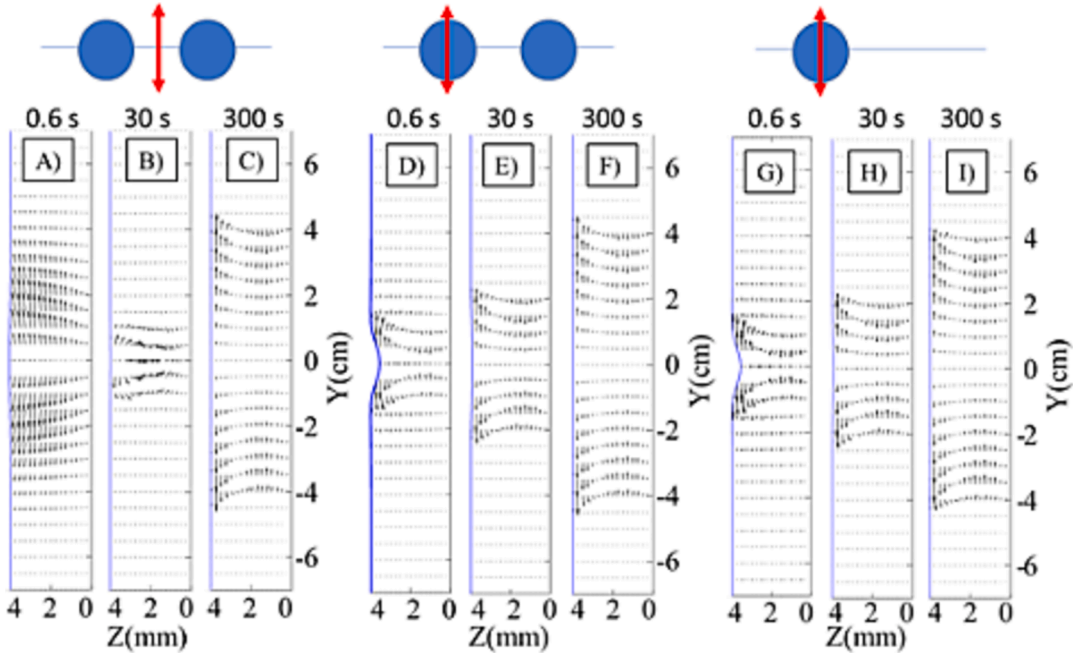

Fig. 7. Flow behavior orthogonal to the centerline. The early interaction regime (0.6 s) is shown in A, D, and G. The late interaction regime (30 s) is shown in B, E, and H, and the quasi-one disk regime (300 s) is shown in C, F, and I. The orientation and locus for each set of flowfields is designated by the corresponding diagram. A, B, and C show the profile along the midline; D, E, and F show the profiles along the orthogonal direction at the disk center for the two disk case, and G, H, and I show the corresponding flowfield for the one disk case. Arrows on a single subfigure are proportional the flow velocity in that subfigure but should not be compared between subfigures. Largest arrows in each panel correspond to A: $4.1\text{x}10^{-5}$ m/s, B: $3.0\text{x}10^{-5}$ m/s, C: $4.8\text{x}10^{-6}$ m/s, D: $1.5\text{x}10^{-3}$ m/s, E: $8.6\text{x}10^{-5}$ m/s, F: $1.4\text{x}10^{-5}$ m/s, G: $1.5\text{x}10^{-3}$ m/s, H: $8.6\text{x}10^{-5}$ m/s, I: $1.3\text{x}10^{-5}$ m/s.

through the center of a disk in the orthogonal direction in the two-disk case (Fig. 7F) and the one that developed for the one disk case (Fig. 7I). In this way, the flow fields in the orthogonal direction at the midpoint of the two disks at long times were similar to the orthogonal flow fields through the center of the disk in the one disk case. The flow along the two-disk midline evolves differently from the orthogonal flow field centered on a disk, but recirculation flows centered on the midpoint eventually develop that closely resemble the orthogonal recirculation flow and the one disk recirculation flow. This sets the stage for the quasi-one disk regime, where the flowfield behaves as if it came from a single source centered at the midpoint.

3.2.2. *Directional dependence of key properties*

The discussion above presented key features at selected times; next we examine the temporal evolution of the features in more detail with respect to different directions. A more holistic way to understand the effect of the second disk on the spreading of the first uses differences between the key properties of the one- and two-disk cases, integrated over the domain of spreading. If we limit our scope to only the left disk ($x < 0$ cm) and compare the results for the one disk case and two disk case, any differences that exist must result from the interaction with the second disk. This is expressed as a total difference

$$\Delta\Xi(t) = \sum_{x,y,z} \sqrt{\xi(t,x,y,z)_{2disk}{}^2 - \xi(t,x,y,z)_{1disk}{}^2} \tag{12}$$

where $\Delta\Xi$ is the total difference of some chosen property, ξ_{2disk} is that property value at a specified x,y, z location for the two disk case, ξ_{1disk} is the property value at the same x, y, z location for the one disk case, and the sum is for all points in the region of interest for ($x < 0$ cm, y, z). To better show the temporal ordering and relative magnitude of the effects of the second disk on the first, we normalize each of the total difference quantities $\Delta\Xi(t)$ by the maximum value of the total difference across all times and directions $\Delta\Xi_{max}$. While these normalized standard differences are important when understanding the ordering of events as a whole (see section 3.2.4 below), normalized total differences can also be taken along specific directions (proximal, orthogonal, and distal) to understand how this ordering changes with direction (Fig. 8).

Fig. 8 shows the normalized total differences for the velocity magnitude, the surface height distortion, and the surface concentration over the course of the simulation for the initial separation $d = 2$ cm case for the proximal (Fig. 8A), orthogonal (Fig. 8B) and distal (Fig. 8C) directions. Each of these properties is affected differently by the second disk. Looking first at the proximal direction, as time proceeds from the independent regime to the interaction regime (marked by Roman numeral I in Fig. 8A), the velocity magnitude total difference is the first property to change. This change is the first significant difference between the one disk and two disk cases and defines where the transition between the independent and interaction regime occurs. Shortly after, at approximately $t = 0.02$ s, this is followed by the onset of the surface height total difference increasing. The total velocity difference then reaches a maximum at $t = 0.6$ s (at Roman numeral II in Fig. 8A), followed shortly thereafter by a maximum in the total height difference, both occurring at nearly the same time as the maximum height at the midpoint (Fig. 3). Both of these total differences then quickly decrease to relatively low values as the surfactant front interaction approaches (at Roman numeral III in 8A, Fig. 4). A local minimum occurs in the total height difference at this time as the surface height goes from being larger for the two disk case (global maximum at the midpoint at Roman Numeral II in 8A) to smaller for the two disk case (global minimum at the midpoint at Roman numeral IV in 8A). During this time we also see a local maximum in the total surface concentration difference (at ~ 3 s), which we will later (section 3.2.3) correlate to the disks being pushed apart by the Marangoni flow.

After the point when the surfactant fronts begin to interact (Roman numeral II in Fig. 8A, Fig. 3), the surface excess concentration difference starts increasing significantly, which is associated with deformation of the surfactant front due to the presence of the second disk. The surface excess concentration total difference reaches a maximum as the surface excess concentration stops increasing at the midpoint between the disks

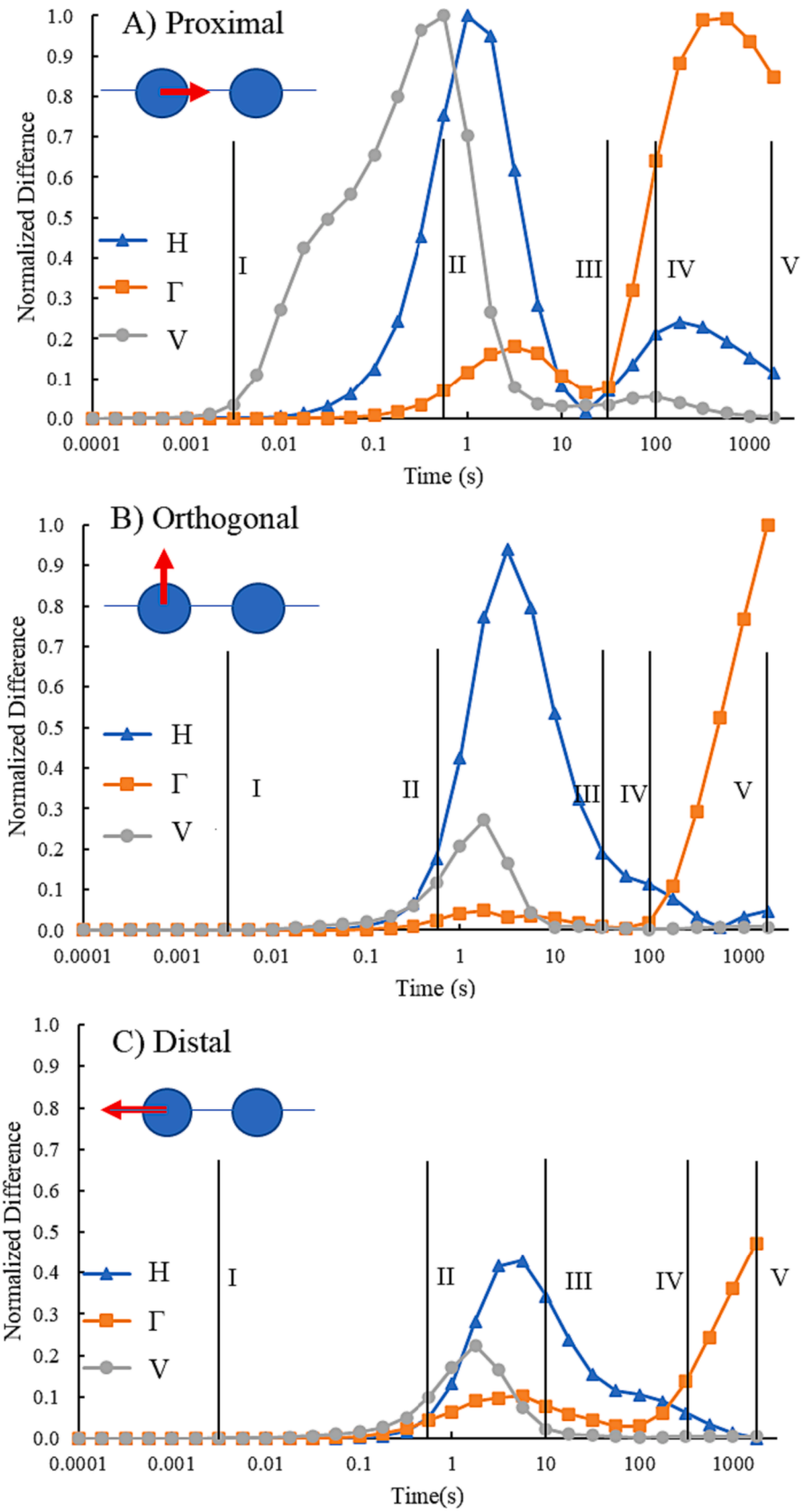

Fig. 8. Normalized total difference for the velocity magnitude (V), surface height (H), and surface concentration (Γ) over the duration of the simulation for the d = 2 cm case in the proximal (A) orthogonal (B) and distal (C) directions. Important times are denoted by the vertical lines and marked with roman numerals I) Onset of interaction regime, II) Maximum height at the midpoint, III) Surfactant front interaction, IV) Minimum height at the midpoint, and V) Onset of the quasi-one disk regime. The onset of the increase in a property difference is defined as when it increases above the baseline by an amount equal to 1 % of the maximum value for that property difference.

and starts decreasing (see Fig. 4D, 6D, and 7D), while the velocity difference has approached zero, and the surface height total difference continues to decrease. In summary, these different properties are most affected by the second disk at different times: first the velocity fields, then the surface deformation, and finally the surfactant surface concentration. Although the timings for when these properties are affected by the second source differ from each other, attempting to interpret this in terms of physical cause-and-effect relations may be oversimplifying since they are inextricably linked in the physics of the coupled transport processes. Furthermore, while the precise timing for when surfactant fronts interact would depend on the definition of the surface concentration marking the location of the front (currently taken as 0.01 % of Γ_{max}), the interpretation of the relative sequence of the various events based on the total property differences $\Delta\Xi$ does not depend on the chosen threshold, and thus conclusions about the sequence of events are robust.

Next, we compare the sequence of events in the proximal direction (Fig. 8A) with the orthogonal (Fig. 8B) and distal (Fig. 8C) directions. For both of these latter directions, the same temporal ordering is observed: first the onset of a difference in velocity, then subphase height, and finally surface concentration. However, the times when each of these property differences become significant occur at later times than for the proximal direction, and the onsets are closer together. This is especially clear for the total height differences where the maximum occurs first for the proximal direction, then the orthogonal direction, and finally the distal direction. This corresponds as expected to the larger distance from the second disk when considering the orthogonal and distal directions. The property differences are mainly smallest in the distal direction and largest in the proximal direction, although there are some exceptions. First, for the local maximum observed in the surface concentration difference, this maximum is larger in the distal direction than the orthogonal direction. This is because this maximum is induced by the disk of surfactant being moved by the Marangoni stresses that originated from the other disk, as will be shown in section 3.2.3. This results in a relatively large effect for the proximal and distal differences as they are in the direction of the shift, but a smaller effect in the direction orthogonal to the translation. Second, for the total surface concentration difference the largest value is for the orthogonal direction at late times. This is a result of the surface excess concentration at the midpoint reaching a maximum and starting to decrease again (getting closer to the one disk case value) for the proximal direction, while deformation of the surfactant front results in a higher concentration in the orthogonal direction that only continues to increase (see next section).

3.2.3. *Measures of surface transport*

Next, we consider the origin of the two experimentally observed phenomena discussed in the introduction: the disks spreading apart from one another and the disks deforming each other (Figures S1 and S2). Fig. 9A shows the displacement of the center of mass of the left disk ($x < 0$), calculated as

$$x_{COM} = \frac{1}{M_{tot}} \sum m_i x_i \tag{13}$$

where x_{COM} is the location of the center of mass of the surfactant distribution, M_{tot} is the total mass of surfactant in the system, m_i is the mass of surfactant associated with a single area element on the interface, and x_i is the distance from the original disk center along the midline. The center of mass displacement is $x_{COM}(t) - x_{COM}(t_o)$. Across all tested initial separation distances, two key features emerge as shown in Fig. 9: first, a local maximum in center of mass displacement and second, a sharp increase in the center of mass displacement at later times. As the initial separation distance between the disk edges (d) is increased, all features of the plot are delayed to later times.

The center of mass is sensitive to both translation of the disk and deformation of the disk, so a second measurement, the circularity C is needed to distinguish the two effects:

$$C = \frac{4\pi A}{P^2} \tag{14}$$

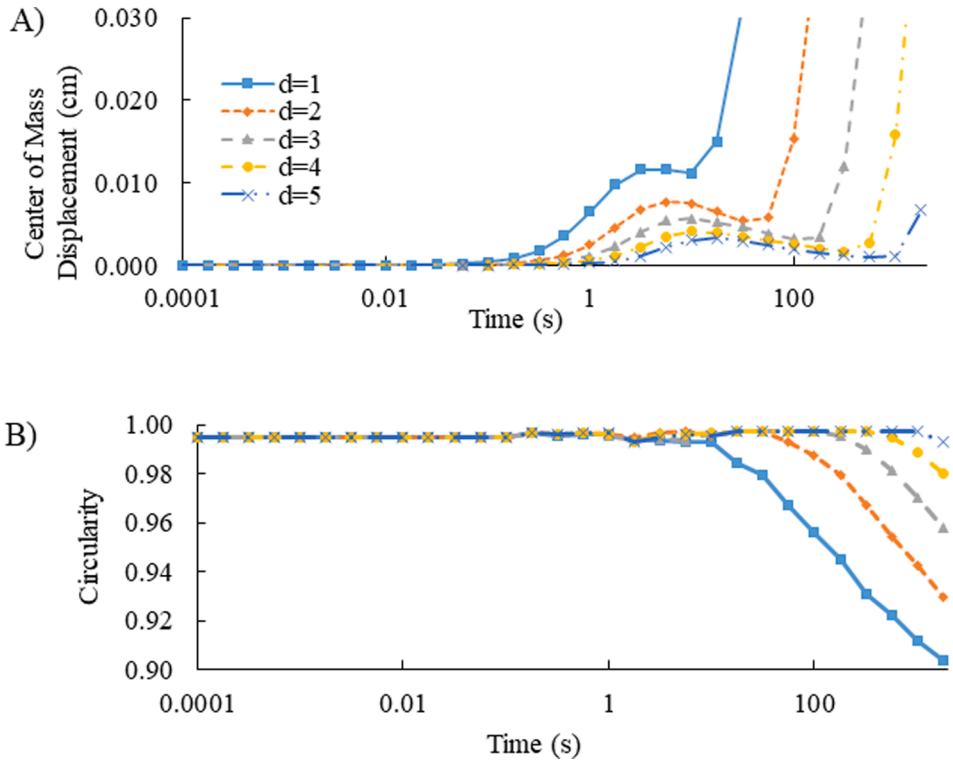

Fig. 9. The center of mass displacement A) and circularity B) of the left disk for $d = 1$, 2, 3, 4, and 5 cm. The onset of change in center of mass displacement is defined to occur at the time point just before the displacement becomes greater than 10 μm. The onset of change in circularity is defined as when it decreases below 0.99.

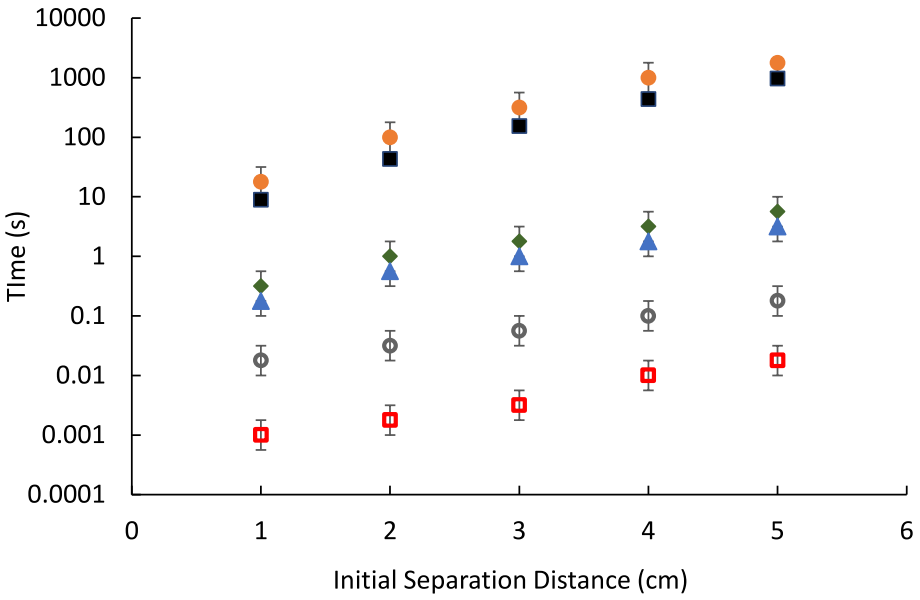

Fig. 10. Ordering of significant events in time: This includes initial increase in total velocity difference (□) [Fig. 8], initial increase in total height difference (○) [Fig. 8], onset of center of mass displacement (▲) [Fig. 9A], initial increase in total surface concentration difference (◆) [Fig. 8], time of surfactant front interaction (■) [Fig. 4], and onset of change in circularity (●) [Fig. 9B].

where A is the area bounded within the surfactant front, and P is the perimeter of the surfactant front. Circularity is 1 for a circle, and decreasing values indicating deviation from a circle. Circularity can only measure deformations to the surfactant disk and not translations. Fig. 9B shows that while there was no longer a local extremum at early times as there was in the center of mass displacement, the circularity changed abruptly at later times that coincided with the large increase in center of mass displacement. In all cases, the change in circularity began after the center of mass displacement had already begun. This alignment of temporal effects on center of mass displacement and circularity occurred for each initial disk separation distance. This indicates that the local maxima in center of mass displacement (Fig. 9A) are not caused by a deformation of the disk, but instead by motion of the disks away from each other. This manifests as an effective repulsion that results from the Marangoni flow fields.

3.2.4. *Impact of initial separation distance on overall timing of events*

Fig. 10 summarizes when the key events occur, and how this timing is affected by changing the initial disk separation distance. These events can be separated into four main groups. Regardless of initial separation distance, the first event is the interaction of the disk velocity fields, followed by the distortion of the surface height profile. This is followed by the center of mass displacement, which is closely followed in time by the total change in the surface concentration field. Finally, the surfactant fronts begin to interact, followed closely in time by the change in circularity. These groupings are significantly separated in time. Translation of the surfactant disk centers of mass is directly associated with the interacting velocity fields and precedes the direct surfactant front interaction. The latter is more closely associated with the change in circularity of the disks. The relative ordering of all these events remains the same for increasing initial separation distance. The sensitivity of the onset times to initial separation distance is significant: a five-fold increase in initial distance can produce up to a two order of magnitude delay in onset times.

4. Conclusions

Solutal Marangoni spreading from multiple sources is relevant to many applications including spray coating and lung disease treatment. Here we have modeled the interaction of two spreading surfactant disks, in order to start to bridge the gap between the single source[6,7] and multi-source Marangoni spreading research literature[16,17]. This work has elucidated the cause of the mutual distortion and the effective repulsion of interacting surfactant sources previously noted in multi-source surfactant spreading experiments.

The interaction of two Marangoni spreading sources occurs in three distinct regimes: the independent regime in which two spreading disks behave similarly to a single disk with no significant interaction between them, the interaction regime where velocity fields originating from the two disks interact and are associated with significant alterations in surface deformation and surface concentration fields compared to spreading from a single source, and finally the quasi-one disk regime where the spreading fields effectively merge and exhibit spreading characteristics that resemble those of a single source.

During the interaction regime, the presence of the second disk first makes a noticeable change in the velocity fields and then the surface deformation until the surface height at the midpoint between the disks reaches a maximum. At this point, a recirculation flow has developed in the bulk liquid centered around the initial center of the surfactant disks. This is associated with a displacement of the disk centers of mass, indicating the surfactant disks are being pushed apart from each other. Eventually, the surfactant fronts touch and only then do significant changes in the shape of the spreading disks occur.

In the quasi-one disk regime, the spreading features of the two disks merge with a new center at the original midpoint between the two disks. The two recirculation flows that had originated from each disk have now merged and become centered around the midpoint between the disks rather than the initial disk centers. All behaviors described here occur similarly for each separation distance studied. Increasing the initial separation distance significantly increases the onset time but preserves the relative temporal ordering of each key event in the two-disk interaction. While the numerical modeling results reported here help elucidate the origin of visual observations in multi-source surfactant spreading, this work should motivate future flow visualization experiments[16,17] to directly test the detailed predictions of the two-source model.

CRediT authorship contribution statement

Steven Iasella: Conceptualization, Methodology, Software, Formal analysis, Investigation, Writing – original draft, Writing – review & editing. **Ramankur Sharma:** Conceptualization, Writing – review & editing. **Stephen Garoff:** Conceptualization, Methodology, Writing – original draft, Writing – review & editing, Supervision, Funding acquisition. **Robert D. Tilton:** Conceptualization, Methodology, Writing – original draft, Writing – review & editing, Supervision, Funding acquisition.

Declaration of Competing Interest

The authors declare that they have no known competing financial interests or personal relationships that could have appeared to influence the work reported in this paper.

Data availability

Data will be made available on request.

Acknowledgements

This material is based on work supported by the National Science Foundation under grants CBET-1510293 and CBET-0931057. The authors thank Minkyoung Kim for experimental imaging of impinging surfactant solutions.

Appendix A. Supplementary data

Supplementary data to this article can be found online at https://doi.org/10.1016/j.jcis.2023.09.109.

References

[1] D.W. Fallest, A.M. Lichtenberger, C.J. Fox, K.E. Daniels, Fluorescent visualization of a spreading surfactant, New J. Phys. 12 (2010).
[2] Swanson, E. R., Strickland, S. L., Shearer, M. & Daniels, K. E. Surfactant Spreading on a Thin Liquid Film: Reconciling Models and Experiments. (2013).
[3] R. Sharma, et al., Quasi-immiscible spreading of aqueous surfactant solutions on entangled aqueous polymer solution subphases, ACS Appl. Mater. Interfaces 5 (2013) 5542–5549.
[4] X. Wang, E. Bonaccurso, J. Venzmer, S. Garoff, Deposition of drops containing surfactants on liquid pools: Movement of the contact line, Marangoni ridge, capillary waves and interfacial particles, Colloids Surf A Physicochem Eng Asp 486 (2015) 53–59.
[5] R. Sharma, T.E. Corcoran, S. Garoff, T.M. Przybycien, R.D. Tilton, Transport of a partially wetted particle at the liquid/vapor interface under the influence of an externally imposed surfactant generated Marangoni stress, Colloids Surf A Physicochem Eng Asp 521 (2017) 49–60.
[6] A.B. Afsar-Siddiqui, P.F. Luckham, O.K. Matar, The spreading of surfactant solutions on thin liquid films, Adv. Colloid Interface Sci. 106 (2003) 183–236.
[7] D.P. Gaver, J.B. Grotberg, The dynamics of a localized surfactant on a thin film, J. Fluid Mech. 213 (1990) 127.
[8] D.P. Gaver, J.B. Grotberg, Droplet spreading on a thin viscous film, J. Fluid Mech. 235 (1992) 399.
[9] O.K. Matar, R.v. Craster, Dynamics of surfactant-assisted spreading, Soft Matter 5 (2009) 3801.
[10] G. Karapetsas, R.V. Craster, O.K. Matar, Surfactant-driven dynamics of liquid lenses, Phys. Fluids 23 (2011), 122106.
[11] J.G. Lee, L.L. Larive, K.T. Valsaraj, B. Bharti, Binding of lignin nanoparticles at oil-water interfaces: An ecofriendly alternative to oil spill recovery, ACS Appl. Mater. Interfaces 10 (2018) 43282–43289.
[12] S.v. Iasella, et al., Aerosolizing lipid dispersions enables antibiotic transport across mimics of the lung airway surface even in the presence of pre-existing lipid monolayers, J. Aerosol Med. Pulm. Drug Deliv. 31 (2018) 212–220.
[13] S.V. Iasella, et al., Flow regime transitions and effects on solute transport in surfactant-driven Marangoni flows, J. Colloid Interface Sci. 553 (2019) 136–147.
[14] T.L. Hsieh, S. Garoff, R.D. Tilton, Marangoni spreading time evolution and synergism in binary surfactant mixtures, J. Colloid Interface Sci. 623 (2022) 685–696.
[15] M.L. Sauleda, T.L. Hsieh, W. Xu, R.D. Tilton, S. Garoff, Surfactant spreading on a deep subphase: Coupling of Marangoni flow and capillary waves, J. Colloid Interface Sci. 614 (2022) 511–521.
[16] R. Sharma, et al., Surfactant driven post-deposition spreading of aerosols on complex aqueous subphases. 2: Low deposition flux representative of aerosol delivery to small airways, J. Aerosol Med. Pulm. Drug Deliv. 28 (2015) 394–405.
[17] A. Khanal, et al., Surfactant driven post-deposition spreading of aerosols on complex aqueous subphases. 1: High deposition flux representative of aerosol delivery to large airways, J. Aerosol Med. Pulm. Drug Deliv. 28 (2015) 382–393.
[18] H. Kim, et al., Controlled uniform coating from the interplay of marangoni flows and surface-adsorbed macromolecules, Phys. Rev. Lett. 116 (2016), 124501.
[19] D. Kang, A. Nadim, M. Chugunova, Marangoni effects on a thin liquid film coating a sphere with axial or radial thermal gradients, Phys. Fluids 29 (2017), 072106.
[20] Z. Liu, et al., Vapor-induced marangoni coating for organic functional films, J Mater Chem C Mater 9 (2021) 17518–17525.
[21] J.L. Bull, et al., Surfactant-spreading and surface-compression disturbance on a thin viscous film, J. Biomech. Eng. 121 (1999) 89–98.
[22] J.B. Grotberg, D. Halpern, O.E. Jensen, Interaction of exogenous and endogenous surfactant: spreading-rate effects, J. Appl. Physiol. 78 (1995) 750–756.
[23] Y.L. Zhang, O.K. Matar, R.V. Craster, A theoretical study of chemical delivery within the lung using exogenous surfactant, Med. Eng. Phys. 25 (2003) 115–132.
[24] M.L. Sauleda, H.C.W. Chu, R.D. Tilton, S. Garoff, Surfactant driven marangoni spreading in the presence of predeposited insoluble surfactant monolayers, Langmuir 37 (2021) 3309–3320.
[25] A.B. Afsar-Siddiqui, P.F. Luckham, O.K. Matar, Unstable spreading of aqueous anionic surfactant solutions on liquid films. 2. Highly soluble surfactant, Langmuir 19 (2003) 703–708.
[26] S. Le Roux, M. Roché, I. Cantat, A. Saint-Jalmes, Soluble surfactant spreading: How the amphiphilicity sets the Marangoni hydrodynamics, Phys. Rev. E Stat. Nonlin. Soft Matter Phys. 93 (2016) 1–13.
[27] K.S. Lee, V.M. Starov, Spreading of surfactant solutions over thin aqueous layers at low concentrations: Influence of solubility, J. Colloid Interface Sci. 329 (2009) 361–365.
[28] Y.L. Zhang, O.K. Matar, R.V. Craster, Surfactant spreading on a thin weakly viscoelastic film, J. Nonnewton. Fluid Mech. 105 (2002) 53–78.
[29] R.V. Craster, O.K. Matar, Numerical simulations of fingering instabilities in surfactant-driven thin films, Phys. Fluids 18 (2006).
[30] M.R.E. Warner, R.V. Craster, O.K. Matar, Fingering phenomena created by a soluble surfactant deposition on a thin liquid film, Phys. Fluids 16 (2004) 2933–2951.
[31] K.S. Lee, N. Ivanova, V.M. Starov, N. Hilal, V. Dutschk, Kinetics of wetting and spreading by aqueous surfactant solutions, Adv. Colloid Interface Sci. 144 (2008) 54–65.
[32] A. Nepomnyashchy, Droplet on a liquid substrate: Wetting, dewetting, dynamics, instabilities, Curr. Opin. Colloid Interface Sci. 51 (2021), 101398.
[33] W. Sun, F. Yang, Contact interaction of two oil lenses floating on surface of deionized water, Langmuir 34 (2018) 11992–12001.
[34] W. Tewes, M.A. Hack, C. Datt, G.G. Peng, J.H. Snoeijer, Theory for the coalescence of viscous lenses, J. Fluid Mech. 928 (2021) A11.
[35] M.A. Hack, et al., Self-similar liquid lens coalescence, Phys. Rev. Lett. 124 (2020), 194502.
[36] D.K.N. Sinz, M. Hanyak, A.A. Darhuber, Immiscible surfactant droplets on thin liquid films: Spreading dynamics, subphase expulsion and oscillatory instabilities, J. Colloid Interface Sci. 364 (2011) 519–529.
[37] K. Koch, B. Dew, T.E. Corcoran, T.M. Przybycien, R.D. Tilton, S. Garoff, Surface tension gradient driven spreading on aqueous mucin solutions: a posible route to enhanced pulmonary drug delivery, Mol. Pharm. 8 (2011) 387–394.
[38] C.H. Huang, M.S. Carvalho, S. Kumar, Stretching liquid bridges with moving contact lines: Comparison of liquid-transfer predictions and experiments, Soft Matter 12 (2016) 7457–7469.
[39] The finite element method (FEM). *Multiphysics Cyclopedia*, COMSOL, comsol.com/multiphysics.